

Adaptive Multi-Order Graph Regularized NMF with Dual Sparsity for Hyperspectral Unmixing

Hui Chen, *Member, IEEE*, Liangyu Liu, Xianchao Xiu, and Wanquan Liu, *Senior Member, IEEE*

Abstract—Hyperspectral unmixing (HU) is a critical yet challenging task in remote sensing. However, existing nonnegative matrix factorization (NMF) methods with graph learning mostly focus on first-order or second-order nearest neighbor relationships and usually require manual parameter tuning, which fails to characterize intrinsic data structures. To address the above issues, we propose a novel adaptive multi-order graph regularized NMF method (MOGNMF) with three key features. First, multi-order graph regularization is introduced into the NMF framework to exploit global and local information comprehensively. Second, these parameters associated with the multi-order graph are learned adaptively through a data-driven approach. Third, dual sparsity is embedded to obtain better robustness, i.e., $\ell_{1/2}$ -norm on the abundance matrix and $\ell_{2,1}$ -norm on the noise matrix. To solve the proposed model, we develop an alternating minimization algorithm whose subproblems have explicit solutions, thus ensuring effectiveness. Experiments on simulated and real hyperspectral data indicate that the proposed method delivers better unmixing results.

Index Terms—Hyperspectral unmixing (HU), nonnegative matrix factorization (NMF), multi-order graph, dual sparsity

I. INTRODUCTION

IN the field of remote sensing, hyperspectral images (HSIs) have attracted extensive attention due to their high spatial and spectral resolution. However, HSIs are usually high-dimensional and noisy, which has led to a series of techniques to extract useful information, such as denoising [1]–[3], classification [4]–[6], anomaly detection [7]–[9], and hyperspectral unmixing (HU) [10]–[12]. Among them, HU plays a critical role in analyzing HSIs by separating spectral endmembers and estimating their abundance fractions, with wide applications in medical diagnostics [13], environmental monitoring [14], and precision agriculture [15].

During the past decades, a large number of methods have emerged to deal with the HU problem under the framework of a linear mixing model (LMM), which can be roughly divided into geometry-based [16], [17], statistics-based [18], [19], regression-based [20], [21], and deep learning-based [22], [23]. Specifically, HU includes two stages: endmember extraction,

such as vertex component analysis (VCA) [24] based on the geometric structure, and abundance estimation, such as fully constrained least squares (FCLS) [25] based on least squares. Actually, VCA-FCLS has been broadly used for initialization in the unmixing process. It is worth noting that nonnegative matrix factorization (NMF) [26], as a statistics-based method, has been recognized as a powerful unmixing tool because of its nonnegative property consistent with the fact that image pixel values are nonnegative while allowing the simultaneous estimation of endmembers and their respective abundances. See [27], [28] for recent surveys about NMF.

To enhance the unmixing performance of NMF, researchers have developed a large number of constrained NMF methods and achieved remarkable results. For example, Miao and Qi [29] incorporated a volume constraint based on the convex cone simplex into the standard NMF and proposed MVC-NMF. Qian et al. [30] suggested $\ell_{1/2}$ -norm [31] constrained NMF to improve the interpretability, which is denoted as SNMF in our paper without ambiguity. Subsequently, Zhu et al. [32] replaced $\ell_{1/2}$ -norm with ℓ_q -norm ($0 < q < 1$) to obtain the ability of adaptive selection [33]. Furthermore, Wang et al. [34] considered the sparse structure of local pixels and combined it with the smoothness constraint, which is called spatial group sparsity regularized NMF (SGSNMF). Besides, there are low-rank constrained NMF [35], [36], abundance separation constrained NMF [37], [38], etc. We would like to point out that although constrained NMF methods significantly improve the performance of traditional NMF by incorporating prior information, it is still not robust to noise and outliers [39], [40]. To this end, Févotte et al. [41] proposed robust NMF (RNMF) by introducing additional sparse matrices to filter out sparsely distributed noise. Recently, Zhang et al. [42] constructed group sparsity constrained NMF, which is denoted as IRNMF. In addition to the above constrained NMF methods, Abdolali et al. [43] transformed the minimum-volume NMF problem in the primal space to a maximum-volume problem in the dual space for a more stable global solution, which is called MV-DUAL. In summary, the above-mentioned sparse constrained NMF methods have good unmixing performance, hence we will continue to align this strategy.

Recently, graph learning was incorporated with NMF to capture the low-dimensional features in HSIs [44], [45]. Lu et al. [46] proposed a graph-regularized NMF method by combining manifold regularization with sparse constrained NMF, where the manifold regularization term was validated to strengthen the connection between original images and abundance maps. Yang et al. [47] considered spatial geometric distance and spectral geometric distance as metrics and obtained

This work was supported in part by the Natural Science Foundation of Shanghai under Grant 24ZR1425700, in part by the National Natural Science Foundation of China under Grant 12371306, and in part by the Project of the State Administration of Foreign Experts under Grant H20240974. (Corresponding author: Xianchao Xiu.)

H. Chen and L. Liu are with the School of Automation Engineering, Shanghai University of Electric Power, Shanghai 200090, China (e-mail: chenhuai@shiep.edu.cn; liangyuliu@mail.shiep.edu.cn).

X. Xiu is with the School of Mechatronic Engineering and Automation, Shanghai University, Shanghai 200444, China (e-mail: xcxiu@shu.edu.cn).

W. Liu is with the School of Intelligent Systems Engineering, Sun Yat-sen University, Guangzhou 510275, China (e-mail: liuwq63@mail.sysu.edu.cn).

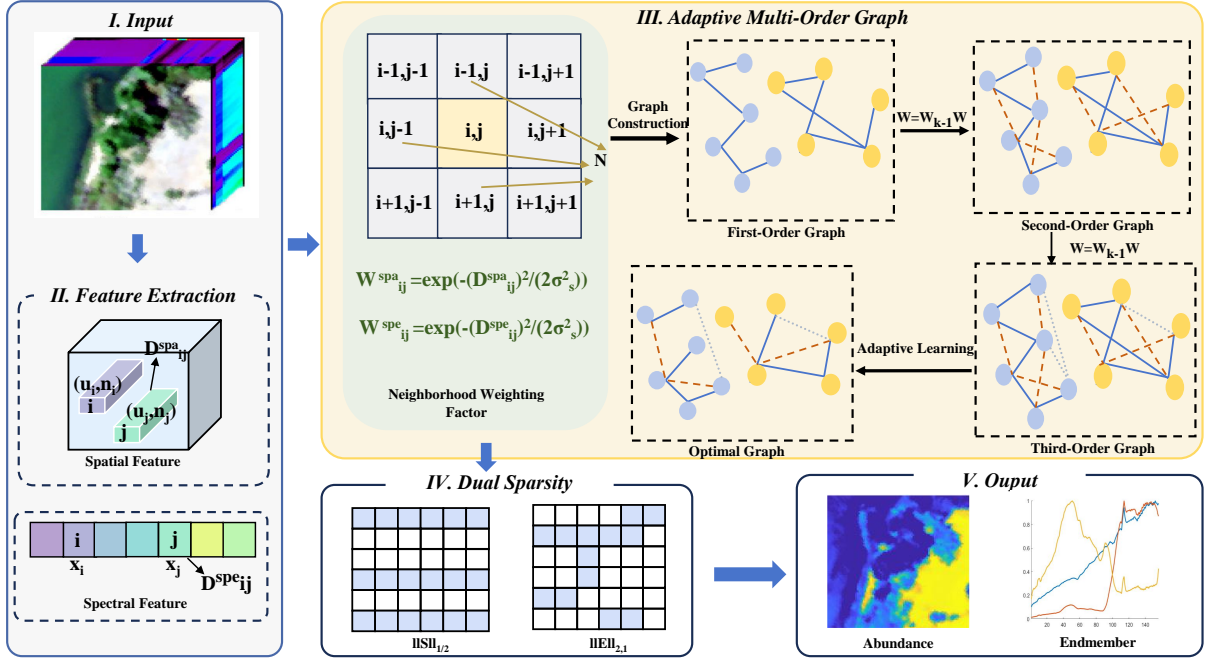


Fig. 1. Flowchart of our proposed method. First, input the HSI. Second, extract spatial and spectral features. Third, construct the multi-order graph, where blue solid lines, yellow dashed lines, and gray dashed lines represent first-order neighbor relationships, second-order neighbor relationships, and third-order neighbor relationships, respectively. Fourth, add dual sparse regularization terms. Finally, output the abundance map and the endmember map.

a space-spectral manifold-regularized NMF model. Wang et al. [48] introduced the hypergraph structure to capture the similarity relationships among spatially neighboring pixels and proposed hypergraph-regularized sparse NMF. Very recently, Qu et al. [49] presented a high-order graph regularized NMF method, called HGNMF-FS. However, these graph learning-based methods have two limitations. On the one hand, they mainly focus on first-order or fixed-order neighborhood relations [50]. This may lead to the loss of key pixel association information when applied to HSIs with complex distributions, thereby limiting the model's ability to represent global and local structures. On the other hand, their graph construction always relies on the predefined parameters and lacks the ability to adaptively learn graph structures.

Motivated by the studies mentioned above, we propose a novel robust and adaptive multi-order graph regularized NMF method for HU. As illustrated in Fig. 1, this method can adaptively learn spatial and spectral graph structures according to the characteristics of the input HSIs, thereby efficiently capturing data features. In addition, dual sparse regularization terms are incorporated to enhance reliability, i.e., $\ell_{1/2}$ -norm on the abundance matrix and $\ell_{2,1}$ -norm on the noise matrix. In summary, the main contributions of this article are as follows.

- 1) We introduce multi-order graphs to capture the similarity between pixels by defining spatial and spectral geometric distance, thereby solving the problem that existing unmixing methods only rely on single-order nearest neighbor relations and cannot fully capture the complex relationship between pixels in HSIs.
- 2) We design an adaptive strategy to learn the weights of multi-order graphs and leverage regularization techniques

to avoid overfitting. On this basis, we further incorporate dual sparsity into the NMF framework and finally establish a novel HU method.

- 3) We develop an efficient alternating minimization algorithm whose subproblems can be easily calculated by fast solvers. Extensive experiments on simulated and real HSIs verify the effectiveness of the proposed method and the necessity of multi-order graphs.

The remainder of this article is organized as follows. Section II introduces the notations and related works. Section III describes the proposed model in detail. Section IV outlines its optimization algorithm. Section V provides the experimental results. Section VI concludes this article.

II. PRELIMINARIES

A. Notations

In this paper, matrices are denoted by bold capital letters, vectors by boldface characters, and scalars by lowercase letters. Let \mathbb{R}^D and $\mathbb{R}^{M \times N}$ refer to the sets of all D -dimensional vectors and $M \times N$ -dimensional matrices, respectively. The i -th element of a vector $\mathbf{x} \in \mathbb{R}^D$ is written as x_i . For a matrix $\mathbf{X} \in \mathbb{R}^{M \times N}$, X_{ij} denotes its ij -th element, with \mathbf{x}^i and \mathbf{x}_j indicating the i -th row and the j -th column, respectively. The transpose of \mathbf{X} is written as \mathbf{X}^\top and the trace is $\text{Tr}(\mathbf{X})$. In addition, the Frobenius norm is denoted by $\|\mathbf{X}\|_F$, and the $\ell_{1/2}$ -norm and $\ell_{2,1}$ -norm are, respectively, defined by

$$\|\mathbf{X}\|_{1/2} = \sum_{i=1}^M \sum_{j=1}^N |X_{ij}|^{1/2}, \quad \|\mathbf{X}\|_{2,1} = \sum_{i=1}^M \|\mathbf{x}^i\|_2. \quad (1)$$

B. Linear Mixing Model

Assume that the spectral response of a pixel is a mixture of multiple endmembers, where the proportion of each endmember corresponds to its abundance, the linear mixing model (LMM) can be characterized by

$$\mathbf{X} = \mathbf{A}\mathbf{S} + \mathbf{E}, \quad (2)$$

where $\mathbf{X} = [\mathbf{x}_1, \dots, \mathbf{x}_N] \in \mathbb{R}^{L \times N}$ is the spectral matrix that consists of all pixel spectral vectors, with L and N being the number of spectral bands and pixels, respectively. $\mathbf{A} \in \mathbb{R}^{L \times M}$ is the endmember matrix, where M represents the total number of endmembers. $\mathbf{S} \in \mathbb{R}^{M \times N}$ is the abundance matrix, which describes the proportion of each endmember within each pixel. $\mathbf{E} \in \mathbb{R}^{L \times N}$ is the noise matrix.

As for LMM, the abundances should satisfy the abundance nonnegativity constraint (ANC) and the abundance sum-to-one constraint (ASC). Specifically, ANC requires that each element in the abundance vector of each pixel must be nonnegative, because the abundances of different materials represent their contribution rates and cannot be negative. ASC requires that the sum of all elements in the abundance vector of each pixel must be one, because the total abundance of each material should completely cover the spectral response of the pixel.

C. Nonnegative Matrix Factorization

Under the assumption of LMM, nonnegative matrix factorization (NMF) is a popular method for solving HU problems. Given a nonnegative matrix $\mathbf{X} \in \mathbb{R}^{L \times N}$, NMF aims to decompose it into two nonnegative matrices, i.e., $\mathbf{A} \in \mathbb{R}^{L \times M}$ and $\mathbf{S} \in \mathbb{R}^{M \times N}$, where $M < \min(L, N)$. The mathematical model can be described as

$$\begin{aligned} \min_{\mathbf{A}, \mathbf{S}} \quad & \frac{1}{2} \|\mathbf{X} - \mathbf{A}\mathbf{S}\|_F^2 \\ \text{s.t.} \quad & \mathbf{A} \geq 0, \mathbf{S} \geq 0. \end{aligned} \quad (3)$$

In order to deal with the above problem, an effective alternating iterative method is proposed, called the multiplicative update rule (MUR) [51], i.e.,

$$\begin{aligned} \mathbf{A} &\leftarrow \mathbf{A} * (\mathbf{X}\mathbf{S}^\top) ./ (\mathbf{A}\mathbf{S}\mathbf{S}^\top), \\ \mathbf{S} &\leftarrow \mathbf{S} * (\mathbf{A}^\top \mathbf{X}) ./ (\mathbf{A}^\top \mathbf{A}\mathbf{S}), \end{aligned} \quad (4)$$

where the operator $*$ and $./$ represent element-wise multiplication and division, respectively.

Since it is a nonconvex problem, there may exist some local optimal solutions. As a result, when applying NMF to practical problems, it is necessary to consider the physical meanings of \mathbf{A} and \mathbf{S} , and add the corresponding constraints in the objective function to align with these meanings.

D. Graph Constrained NMF

It is well known that graph learning can be used to project high-dimensional data into a low-dimensional subspace while preserving the geometric relationship between data points. HGNNMF-FS, as a representative constrained NMF method, integrates high-order graph regularization, adaptive feature

selection, and $\ell_{1/2}$ -norm regularization into the NMF framework, which can be expressed as

$$\begin{aligned} \min_{\mathbf{A}, \mathbf{S}, \mathbf{\Lambda}} \quad & \frac{1}{2} \|\mathbf{A}(\mathbf{X} - \mathbf{A}\mathbf{S})\|_F^2 + \gamma \|\mathbf{S}\|_{1/2} + \frac{\lambda}{2} \text{Tr}(\mathbf{S}\mathbf{L}_h\mathbf{S}^\top) \\ \text{s.t.} \quad & \mathbf{A} \geq 0, \mathbf{S} \geq 0, \mathbf{\Lambda} \geq 0, \mathbf{1}_R^\top \mathbf{S} = \mathbf{1}_N^\top. \end{aligned} \quad (5)$$

Note that $\mathbf{L}_h = \beta_1 \mathbf{L}_1 + \beta_2 \mathbf{L}_2$, where \mathbf{L}_1 and \mathbf{L}_2 represent the first-order and second-order Laplacian matrices, respectively, and β_1, β_2 are the parameters. Besides, $\mathbf{\Lambda}$ can be adaptively adjusted during the unmixing process as stated in [49].

III. THE PROPOSED MODEL

This section first describes spatial and spectral graphs, then proposes a novel multi-order graph framework, followed by our proposed model for the HU task.

A. Spatial and Spectral Graphs

Generally speaking, spatial graphs are used to measure the spatial similarity between pixels, and spectral graphs are used to quantify the spectral similarity between pixels, thus they can provide complementary information to better capture the global and local structures of HSIs.

Given two pixels x_i and x_j with spatial coordinates (u_i, n_i) and (u_j, n_j) , respectively, their Euclidean distance and the corresponding weight matrix are typically derived using the following heat kernel function

$$\begin{aligned} D_{ij}^{\text{spa}} &= \sqrt{(u_i - u_j)^2 + (n_i - n_j)^2}, \\ W_{ij}^{\text{spa}} &= \exp\left(- (D_{ij}^{\text{spa}})^2 / (2\sigma_s^2)\right), \end{aligned} \quad (6)$$

where σ_s is the spatial scaling parameter that controls the influence of distance between neighboring pixels. In this way, the spatial map can capture the local spatial structure of pixels, while Gaussian weighting can smooth the similarity between neighboring pixels.

Considering the spectral vectors \mathbf{x}_i and \mathbf{x}_j , their Euclidean distance and spectral weight matrices are usually given by

$$\begin{aligned} D_{ij}^{\text{spe}} &= \|\mathbf{x}_i - \mathbf{x}_j\|_2, \\ W_{ij}^{\text{spe}} &= \exp\left(- (D_{ij}^{\text{spe}})^2 / (2\sigma_l^2)\right), \end{aligned} \quad (7)$$

where σ_l is the spectral scaling parameter that controls the range of spectral similarity. The Gaussian kernel ensures that pixels with high spectral similarity receive higher weights, while different pixels have less influence on unmixing.

Therefore, the corresponding first-order Laplacian matrices of the spatial and spectral maps are defined as

$$\begin{aligned} \mathbf{L}^{\text{spa}} &= \mathbf{D}^{\text{spa}} - \mathbf{W}^{\text{spa}}, \\ \mathbf{L}^{\text{spe}} &= \mathbf{D}^{\text{spe}} - \mathbf{W}^{\text{spe}}, \end{aligned} \quad (8)$$

where \mathbf{D}^{spa} and \mathbf{D}^{spe} represent diagonal matrices, and their diagonal elements are, respectively, given by

$$D_{ii}^{\text{spa}} = \sum_{j=1}^n W_{ij}^{\text{spa}}, \quad D_{ii}^{\text{spe}} = \sum_{j=1}^n W_{ij}^{\text{spe}}. \quad (9)$$

B. Multi-Order Graph

Although constructing first-order nearest neighbor graphs can achieve a low-dimensional approximation of adjacent pixel representations, such local connectivity constraints often fail to characterize the global information inherent in HSIs, where the similarity between many pixels may extend beyond direct neighbors. In this regard, high-order graphs can be considered to improve the accuracy of HU [52]. Let $\mathbf{W} \in \mathbb{R}^{N \times N}$ denote the first-order graph with N nodes, and the k -order graph \mathbf{W}_k is defined as

$$\mathbf{W}_k = \begin{cases} \mathbf{W}, & k = 1, \\ \mathbf{W}_{k-1}\mathbf{W}, & k > 1. \end{cases} \quad (10)$$

After obtaining \mathbf{W}_k , the corresponding Laplacian matrix can be calculated by

$$\mathbf{L}_k = \mathbf{D}_k - \mathbf{W}_k, \quad (11)$$

where $D_{kii} = \sum_{j=1}^N W_{kij}$. The fused higher-order Laplacian matrix \mathbf{L}_m , degree matrix \mathbf{D}_m , and weight matrix \mathbf{W}_m are

$$\begin{aligned} \mathbf{W}_m &= \beta_1 \mathbf{W}_1 + \beta_2 \mathbf{W}_2 + \cdots + \beta_k \mathbf{W}_k, \\ \mathbf{D}_m &= \beta_1 \mathbf{D}_1 + \beta_2 \mathbf{D}_2 + \cdots + \beta_k \mathbf{D}_k, \\ \mathbf{L}_m &= \beta_1 \mathbf{L}_1 + \beta_2 \mathbf{L}_2 + \cdots + \beta_k \mathbf{L}_k, \end{aligned} \quad (12)$$

where β_1, \dots, β_k are the weight parameters. From both spatial and spectral perspectives, we construct the following spatial and spectral multi-order graph

$$\begin{aligned} \mathbf{W}_m &= \beta_1 \mathbf{W}_1^{\text{spa}} + \beta_2 \mathbf{W}_2^{\text{spa}} + \cdots + \beta_k \mathbf{W}_k^{\text{spa}} \\ &\quad + \eta_1 \mathbf{W}_1^{\text{spe}} + \eta_2 \mathbf{W}_2^{\text{spe}} + \cdots + \eta_k \mathbf{W}_k^{\text{spe}}, \\ \mathbf{D}_m &= \beta_1 \mathbf{D}_1^{\text{spa}} + \beta_2 \mathbf{D}_2^{\text{spa}} + \cdots + \beta_k \mathbf{D}_k^{\text{spa}} \\ &\quad + \eta_1 \mathbf{D}_1^{\text{spe}} + \eta_2 \mathbf{D}_2^{\text{spe}} + \cdots + \eta_k \mathbf{D}_k^{\text{spe}}, \\ \mathbf{L}_m &= \beta_1 \mathbf{L}_1^{\text{spa}} + \beta_2 \mathbf{L}_2^{\text{spa}} + \cdots + \beta_k \mathbf{L}_k^{\text{spa}} \\ &\quad + \eta_1 \mathbf{L}_1^{\text{spe}} + \eta_2 \mathbf{L}_2^{\text{spe}} + \cdots + \eta_k \mathbf{L}_k^{\text{spe}}, \end{aligned} \quad (13)$$

where η_1, \dots, η_k are also the weight parameters. Furthermore, if two pixels exhibit similarity both spatially and spectrally, their abundances should also be similar. Therefore, we propose minimizing the following objective function to characterize this relationship

$$\begin{aligned} &\frac{1}{2} \sum_{i,j=1}^N \|\mathbf{s}_i - \mathbf{s}_j\|_2^2 W_{mij} \\ &= \sum_{i=1}^N \mathbf{s}_i^\top \mathbf{s}_i D_{mii} - \sum_{i,j=1}^N \mathbf{s}_i^\top \mathbf{s}_j W_{mij} \\ &= \text{Tr}(\mathbf{S} \mathbf{D}_m \mathbf{S}^\top) - \text{Tr}(\mathbf{S} \mathbf{W}_m \mathbf{S}^\top) \\ &= \text{Tr}(\mathbf{S} \mathbf{L}_m \mathbf{S}^\top). \end{aligned} \quad (14)$$

C. Our Model

In this paper, we introduce multi-order graphs and robust LMM into the NMF framework, given by

$$\begin{aligned} \min_{\mathbf{A}, \mathbf{S}, \mathbf{E}} \quad & \frac{1}{2} \|\mathbf{X} - \mathbf{E} - \mathbf{A} \mathbf{S}\|_F^2 + \gamma \|\mathbf{S}\|_{1/2} \\ & + \beta \|\mathbf{E}\|_{2,1} + \frac{\lambda}{2} \text{Tr}(\mathbf{S} \mathbf{L}_m \mathbf{S}^\top) \\ \text{s.t.} \quad & \mathbf{A} \geq 0, \mathbf{S} \geq 0, \mathbf{1}_R^\top \mathbf{S} = \mathbf{1}_N^\top, \end{aligned} \quad (15)$$

where γ, β, λ are the regularization parameters. Compared with HGNMF-FS in (5), the advantages of our proposed model are as follows.

- $\text{Tr}(\mathbf{S} \mathbf{L}_m \mathbf{S}^\top)$ exploits multi-order graphs to capture the global and local structures of HSIs.
- The weight parameters associated with \mathbf{L}_m can be tuned adaptively, which will be discussed in Subsection IV-B.
- $\|\mathbf{E}\|_{2,1}$ is enforced to filter out sparse noise and corruptions, thus improving robustness.

Note that our proposed model in (15) can also involve \mathbf{A} to achieve adaptive feature selection, but this is not the focus of the current study.

IV. OPTIMIZATION ALGORITHM

In this section, we provide the update scheme for solving (15) and the learning strategy for parameters in (14).

A. Update Scheme

According to the alternating minimization technique, all the variables $\mathbf{A}, \mathbf{S}, \mathbf{E}$ can be optimized one by one, which will be described in detail.

1) *Update A*: By applying the Lagrangian method, the subproblem can be characterized by

$$\Gamma(\mathbf{A}, \mathbf{Y}) = \frac{1}{2} \|\mathbf{X} - \mathbf{E} - \mathbf{A} \mathbf{S}\|_F^2 + \text{Tr}(\mathbf{Y} \mathbf{A}^\top), \quad (16)$$

where \mathbf{Y} is the Lagrangian multiplier.

The derivative of (16) with respect to \mathbf{A} is

$$\frac{\partial \Gamma(\mathbf{A}, \mathbf{Y})}{\partial \mathbf{A}} = -(\mathbf{X} - \mathbf{E}) \mathbf{S}^\top + \mathbf{A} \mathbf{S} \mathbf{S}^\top + \mathbf{Y}. \quad (17)$$

From the Karush-Kuhn-Tucker (KKT) conditions, it holds

$$-(\mathbf{X} - \mathbf{E}) \mathbf{S}^\top + \mathbf{A} \mathbf{S} \mathbf{S}^\top \cdot \mathbf{A} = 0, \quad (18)$$

which shows that the solution for \mathbf{A} can be expressed by

$$\mathbf{A} \leftarrow \mathbf{A} \cdot ((\mathbf{X} - \mathbf{E}) \mathbf{S}^\top) \cdot / (\mathbf{A} \mathbf{S} \mathbf{S}^\top). \quad (19)$$

2) *Update S*: The corresponding Lagrangian function can be constructed as

$$\begin{aligned} \Psi(\mathbf{S}, \mathbf{Z}) &= \frac{1}{2} \|\mathbf{X} - \mathbf{E} - \mathbf{A} \mathbf{S}\|_F^2 + \gamma \|\mathbf{S}\|_{1/2} \\ &\quad + \frac{\lambda}{2} \text{Tr}(\mathbf{S}^\top \mathbf{L}_m \mathbf{S}) + \text{Tr}(\mathbf{Z} \mathbf{S}^\top), \end{aligned} \quad (20)$$

where \mathbf{Z} is the Lagrangian multiplier.

Taking the derivative of (20) with respect to \mathbf{S} , it has

$$\begin{aligned} \frac{\partial \Psi(\mathbf{S}, \mathbf{Z})}{\partial \mathbf{S}} &= -\mathbf{A}^\top (\mathbf{X} - \mathbf{E}) + \mathbf{A}^\top \mathbf{A} \mathbf{S} \\ &\quad + \frac{\gamma}{2} \mathbf{S}^{-1/2} + \lambda \mathbf{S} \mathbf{L}_m + \mathbf{Z}. \end{aligned} \quad (21)$$

From the KKT conditions, it obtains

$$\begin{aligned} &(-\mathbf{A}^\top (\mathbf{X} - \mathbf{E}) + \mathbf{A}^\top \mathbf{A} \mathbf{S} \\ &\quad + \frac{\gamma}{2} \mathbf{S}^{-1/2} + \lambda \mathbf{S} \mathbf{L}_m) \cdot \mathbf{S} = 0. \end{aligned} \quad (22)$$

This, together with the fact that $\mathbf{L}_m = \mathbf{D}_m - \mathbf{W}_m$, derives the solution as follows

$$\begin{aligned} \mathbf{S} &\leftarrow \mathbf{S} \cdot (\mathbf{A}^\top (\mathbf{X} - \mathbf{E}) + \lambda \mathbf{S} \mathbf{W}_m) \cdot / (\mathbf{A}^\top \mathbf{A} \mathbf{S} \\ &\quad + \frac{\gamma}{2} \mathbf{S}^{-1/2} + \lambda \mathbf{S} \mathbf{D}_m). \end{aligned} \quad (23)$$

Algorithm 1 The procedure for solving (15)

Input: Data matrix $\mathbf{X} \in \mathbb{R}^{L \times N}$, parameters $\mu, \alpha, \beta, \gamma, \lambda$
Initialize: $(\mathbf{A}^0, \mathbf{S}^0, \mathbf{E}^0)$
While not converged **do**

 1: Update \mathbf{A} by (19)

 2: Update \mathbf{S} by (23)

 3: Update \mathbf{E} by (25)

End While
Output: $(\mathbf{A}, \mathbf{S}, \mathbf{E})$

3) *Update E:* After updating \mathbf{A} and \mathbf{S} , the subproblem associated with \mathbf{E} is

$$\min_{\mathbf{E}} \frac{1}{2} \|\mathbf{X} - \mathbf{E} - \mathbf{AS}\|_F^2 + \beta \|\mathbf{E}\|_{2,1}, \quad (24)$$

which admits the following closed-form solution

$$\mathbf{E} \leftarrow \text{soft}_{\beta}(\mathbf{X} - \mathbf{AS}). \quad (25)$$

For ease of expression, let $\mathbf{T} = \mathbf{X} - \mathbf{AS}$. The above soft thresholding operator is defined as

$$\text{soft}_{\beta}(\mathbf{t}^i) = \begin{cases} \frac{\|\mathbf{t}^i\|_2 - \beta}{\|\mathbf{t}^i\|_2} \mathbf{t}^i, & \text{if } \|\mathbf{t}^i\|_2 \geq \beta, \\ 0, & \text{otherwise,} \end{cases} \quad (26)$$

where \mathbf{t}^i is the i -th row of \mathbf{T} , and β is the threshold. See [53] for more illustrations.

Finally, Algorithm 1 summarizes the overall framework for solving (15), where the parameters of multi-order graphs in updating \mathbf{S} can be adaptively learned through Algorithm 2.

B. Parameter Adaptive Learning

To learn \mathbf{W}_m , the following model is proposed

$$\begin{aligned} \min_{\mathbf{H}, \mathbf{W}_m} \quad & \sum_{v=1}^V \sum_{k=1}^K H_{vk} \|\mathbf{W}_m - \mathbf{W}_k^v\|_F^2 \\ & + \mu \|\mathbf{W}_m\|_F^2 + \alpha \|\mathbf{H}\|_F^2 \\ \text{s.t.} \quad & \mathbf{W}_m \geq 0, \mathbf{1}_V^\top \mathbf{H} \mathbf{1}_K = 1, \mathbf{H} \geq 0, \end{aligned} \quad (27)$$

of which \mathbf{W}_k^v represents the k -order graph of the spatial or spectral graph. $\mathbf{H} \in \mathbb{R}^{V \times K}$ is the coefficient matrix, where H_{vk} denotes the corresponding weight of \mathbf{W}_k^v in the consensus graph \mathbf{W}_m . V represents the spatial or spectral graph, with $v = 1$ representing the spatial graph and $v = 2$ representing the spectral graph. In addition, μ and α are the regularization parameters to prevent overfitting.

1) *Update \mathbf{W}_m :* The solution can be simplified as

$$\begin{aligned} \min_{\mathbf{W}_m} \quad & \sum_{v=1}^V \sum_{k=1}^K H_{vk} (\text{Tr}(\mathbf{W}_m^\top \mathbf{W}_m) - 2\text{Tr}(\mathbf{W}_m^\top \mathbf{W}_k^v)) \\ & + \mu \|\mathbf{W}_m\|_F^2 \\ \text{s.t.} \quad & \mathbf{W}_m \geq 0. \end{aligned} \quad (28)$$

Denote the objective as $g(\mathbf{W}_m)$. The gradient is

$$\nabla g(\mathbf{W}_m) = 2(1 + \mu) \mathbf{W}_m - 2 \sum_{v=1}^V \sum_{k=1}^K H_{vk} \mathbf{W}_k^v. \quad (29)$$

Algorithm 2 The procedure for solving (27)

Input: Order K , parameters μ, α
Initialize: $H_{vk} = \frac{1}{2K}$, multi-order graphs via (10)

While not converged **do**

 1: Update \mathbf{W}_m by (30)

 2: Update \mathbf{H} by (32)

End While
Output: $(\mathbf{W}_m, \mathbf{H})$

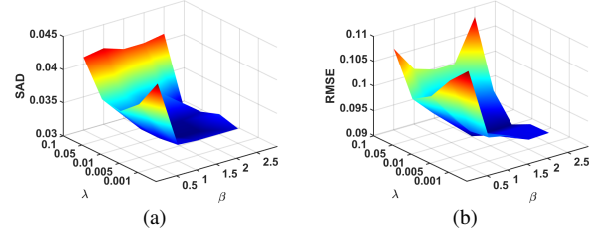


Fig. 2. Parameter sensitivity analysis with respect to λ and β , where (a) SAD and (b) RMSE.

Setting the gradient to zero and considering the constraint $\mathbf{W}_m \geq 0$, the results can be obtained as

$$\mathbf{W}_m \leftarrow \max \left(0, \sum_{v=1}^V \sum_{k=1}^K H_{vk} \mathbf{W}_k^v / (2(1 + \mu)) \right). \quad (30)$$

2) *Update \mathbf{H} :* Let $P_{vk} = \|\mathbf{W}_m - \mathbf{W}_k^v\|_F^2$. Then the subproblem can be written as

$$\begin{aligned} \min_{\mathbf{H}} \quad & \sum_{v=1}^V \sum_{k=1}^K H_{vk} P_{vk} + \alpha \|\mathbf{H}\|_F^2 \\ \text{s.t.} \quad & \mathbf{1}_V^\top \mathbf{H} \mathbf{1}_K = 1, \mathbf{H} \geq 0. \end{aligned} \quad (31)$$

Further, let $\hat{\mathbf{H}} = \text{vec}(\mathbf{H})$ and $\hat{\mathbf{P}} = \text{vec}(\mathbf{P})$. Therefore, the above problem can be reformulated as

$$\min_{\hat{\mathbf{H}}} \quad \alpha \hat{\mathbf{H}}^\top \hat{\mathbf{H}} + \hat{\mathbf{P}}^\top \hat{\mathbf{H}}, \quad (32)$$

which can be solved by existing quadratic programming (QP) solvers.

After obtaining \mathbf{W}_m through Algorithm 2, \mathbf{L}_m and \mathbf{D}_m can be computed using $D_{mii} = \sum_{j=1}^N W_{mij}$ and $\mathbf{L}_m = \mathbf{D}_m - \mathbf{W}_m$, which are then used in Algorithm 1.

V. NUMERICAL EXPERIMENTS

This section presents numerical experiments between our proposed MOGNMF and some state-of-the-art HU methods, including VCA-FCLS [24] [25], MVC-NMF [29], SNMF [30], RNMF [41], SGSNMF [34], IRNMF [42], HGNMF-FS [49], and MV-DUAL [43].

Subsection V-A outlines the experimental setup. Subsection V-B introduces the simulated datasets and their results, while Subsection V-C discusses the real datasets and their results. Subsection V-D provides the ablation experiments. Subsection V-E offers further discussions.

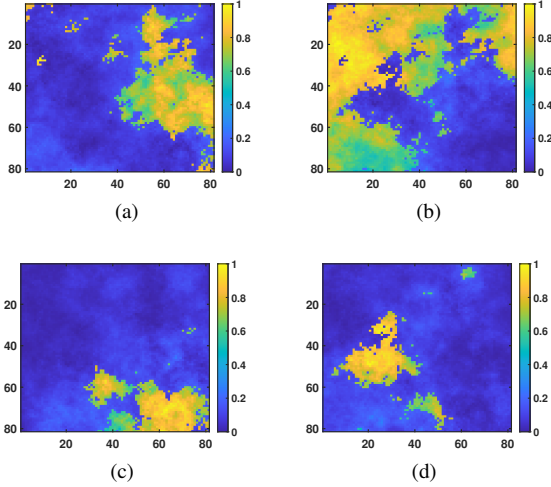


Fig. 3. Illustration of the Simu-1 dataset, where (a)-(d) are the abundance maps in the case of $M = 4$.

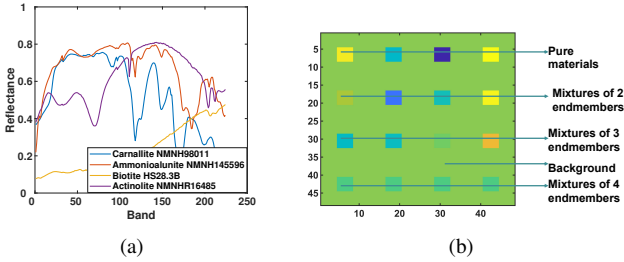


Fig. 4. Illustration of the Simu-2 dataset, where (a) is the spectral signatures of selected endmembers and (b) is the simulated hyperspectral image.

A. Experimental Setup

1) *Parameter Settings*: In the experiments, all compared methods are tested with 20 iterations to ensure the validity and all parameters are chosen according to their literatures. For our proposed MOGNMF, γ , β , and λ should be taken into account. According to [30], γ is estimated by

$$\gamma = \frac{1}{\sqrt{L}} \sum_{l=1}^L \frac{\sqrt{N-1} \|\mathbf{x}^l\|_1}{\|\mathbf{x}^l\|_2 \sqrt{N-1}}, \quad (33)$$

where L represents the number of spectral bands, N represents the total number of pixels, and \mathbf{x}^l represents the vector corresponding to the l -th band in the hyperspectral data $\mathbf{X} \in \mathbb{R}^{L \times N}$. According to Fig. 2, it can be seen that SAD and RMSE exhibit similar variation trends, thus, in subsequent experiments, we set $\beta = 1.5$ and $\lambda = 0.01$. In Algorithm 2, μ is empirically set to 0.01 and α is set to 0.1.

2) *Initializations*: Due to the nonconvexity of problem (15), the initialization of \mathbf{A} and \mathbf{S} significantly impacts the results. Inspired by the existing work, we use VCA-FCLS [24] [25] for initialization. Besides, it is important to satisfy the constraints that both matrices \mathbf{A} and \mathbf{S} are nonnegative (also ANC) and the columns of \mathbf{S} should sum to one (also ASC). In fact, during the iterative process, as long as the initial matrices \mathbf{A} and \mathbf{S} are nonnegative, we can naturally maintain the nonnegativity. The ASC constraint can be implemented using the efficient and

widely used method proposed in [25], where the data matrix $\mathbf{X} - \mathbf{E}$ and the endmember matrix \mathbf{A} are augmented as

$$\overline{\mathbf{X} - \mathbf{E}} = \begin{pmatrix} \mathbf{X} - \mathbf{E} \\ \delta \mathbf{1}_N^\top \end{pmatrix}, \quad \overline{\mathbf{A}} = \begin{pmatrix} \mathbf{A} \\ \delta \mathbf{1}_M^\top \end{pmatrix}, \quad (34)$$

where δ is used to control the effect of ASC. Larger δ values can improve the accuracy, but will also significantly reduce the convergence speed. To balance them, we set $\delta = 15$.

3) *Stopping Criteria*: For Algorithm 1, two stopping criteria are considered. The first is based on a predefined error tolerance. Once the relative error is less than $\epsilon = 10^{-4}$, the iteration stops. The second is the maximum number of iterations, which is set to 3000. The optimization process halts when either of these criteria is satisfied. For Algorithm 2, the maximum number of iterations is 50. The iteration stops when either the maximum number of iterations is reached or the relative error is smaller than 10^{-6} .

4) *Evaluation Metrics*: To evaluate the HU performance of different methods, two popular metrics are employed. For the k -th estimated endmember vector \mathbf{a}_k and its truth endmember $\hat{\mathbf{a}}_k$, the spectral angle distance (SAD) is defined as

$$\text{SAD} = \cos^{-1} \left(\frac{\mathbf{a}_k^\top \hat{\mathbf{a}}_k}{\|\mathbf{a}_k\|_2 \|\hat{\mathbf{a}}_k\|_2} \right). \quad (35)$$

For the k -th estimated abundance vector \mathbf{s}_k and the ground truth abundance vector $\hat{\mathbf{s}}_k$, the root mean square error (RMSE) is given by

$$\text{RMSE} = \sqrt{\frac{1}{N} \sum_{k=1}^N \|\mathbf{s}_k - \hat{\mathbf{s}}_k\|_2^2}. \quad (36)$$

The smaller the SAD and RMSE values, the better the unmixing performance.

B. Results on Synthetic Datasets

1) *Dataset Description*: The Simu-1 dataset is constructed using the hyperspectral imagery synthesis toolbox¹. This toolbox enables control over multiple key parameters, including spatial resolution, endmember spatial distribution patterns, and material composition characteristics. By randomly selecting a varying number of mineral spectra from the U.S. Geological Survey (USGS) digital spectral library as endmembers, where the number of endmembers is denoted as M , their spatial abundance distributions are modeled using Gaussian random fields with radial basis function covariance structures. Fig. 3 presents the abundance maps when $M = 4$.

The Simu-2 dataset is selected from the USGS digital repository², containing reflectance data across 224 spectral channels (0.4-2.5 μm). This dataset is generated under the LMM framework with four materials, see Fig. 4(a). The spatial layout includes discrete geometric regions of pure materials and complex mixtures, as shown in Fig. 4(b).

¹http://www.ehu.es/ccwintco/index.php/Hyperspectral_Imagery_Synthesis_tools_for_MATLAB

²<http://speclab.cr.usgs.gov/spectral.lib06>

TABLE I

SAD VALUES OF DIFFERENT METHODS ON THE SIMU-1 DATASET, WHERE THE TOP TWO VALUES ARE MARKED AS **RED** AND **BLUE**, RESPECTIVELY.

Cases	VCA-FCLS	MVC-NMF	SNMF	RNMF	SGSNMF	IRNMF	HGNMF-FS	MV-DUAL	MOGNMF
SNR=10	0.0968	0.0356	0.0442	0.0627	0.0358	0.0361	0.0438	0.0982	0.0320
SNR=20	0.0821	0.0350	0.0524	0.0610	0.0436	0.0340	0.0331	0.0443	0.0313
SNR=30	0.0321	0.0109	0.0467	0.0508	0.0468	0.0119	0.0319	0.0320	0.0099
SNR=40	0.0122	0.0090	0.0460	0.0149	0.0393	0.0076	0.0267	0.0335	0.0063
Average	0.0558	0.0226	0.0473	0.0473	0.0432	0.0224	0.0338	0.0520	0.0202

TABLE II

RMSE VALUES OF DIFFERENT METHODS ON THE SIMU-1 DATASET, WHERE THE TOP TWO VALUES ARE MARKED AS **RED** AND **BLUE**, RESPECTIVELY.

Cases	VCA-FCLS	MVC-NMF	SNMF	RNMF	SGSNMF	IRNMF	HGNMF-FS	MV-DUAL	MOGNMF
SNR=10	0.0943	0.0966	0.0988	0.0932	0.0944	0.0935	0.1180	0.1517	0.0899
SNR=20	0.0924	0.0937	0.1008	0.1151	0.0941	0.0955	0.0925	0.1276	0.0917
SNR=30	0.0552	0.0310	0.0894	0.0600	0.0599	0.0533	0.0515	0.0475	0.0276
SNR=40	0.0391	0.0319	0.0916	0.0392	0.0881	0.0376	0.0619	0.0462	0.0219
Average	0.0703	0.0633	0.0952	0.0769	0.0841	0.0700	0.0810	0.0933	0.0578

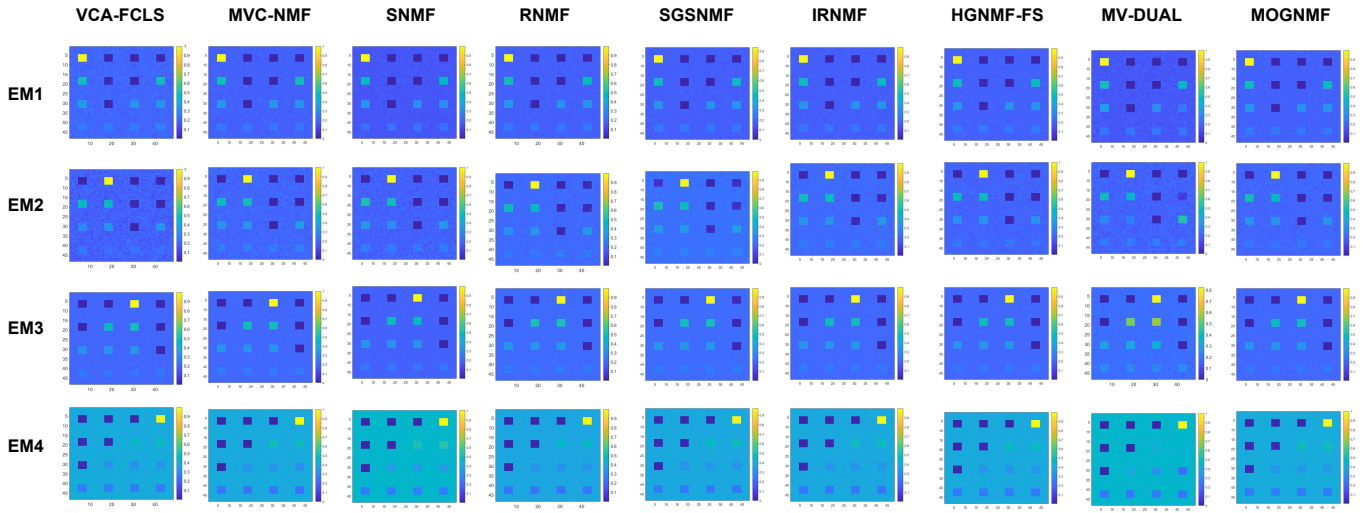


Fig. 5. Abundance maps obtained by the different unmixing methods on the Simu-2 dataset.

2) *Numerical Results:* To emulate real acquisition conditions, the synthetic hyperspectral cubes are corrupted with additive noise calibrated to specific signal-to-noise ratios (SNRs). The SNR quantification follows

$$\text{SNR} = 10 \log_{10} \frac{\mathbb{E}[\mathbf{x}^T \mathbf{x}]}{\mathbb{E}[\mathbf{n}^T \mathbf{n}]}, \quad (37)$$

where \mathbf{x} represents the noise-free signal vector, \mathbf{n} represents the noise vector, and $\mathbb{E}[\cdot]$ denotes the mathematical expectation over all image pixels.

Tables I and II provide the average SAD and RMSE results on the Simu-1 dataset contaminated by Gaussian white noise under SNR = 10, 20, 30 and 40 dB, respectively, where the top two values are marked as **red** and **blue**. It can be observed that when the SNR increases, the unmixing accuracy of all methods improves. Furthermore, compared with HGNMF-FS and RNMF, the proposed MOGNMF demonstrates superior performance under different SNR conditions. This indicates that the introduction of dual sparsity enhances robustness and

also highlights the significant advantages of multi-order graph learning.

Fig. 5 presents the abundance maps obtained by different unmixing methods on the Simu-2 dataset with SNR = 30 dB, where EM1-EM4 denote the selected endmembers. In addition, Fig. 6 shows the abundance maps of the endmember 1 under different noise levels. It can be concluded that, under different SNR conditions, the proposed MOGNMF can generate smoother abundance maps compared with other methods. Even in the case of high noise, the proposed method can still accurately estimate the land cover distribution, which shows its robustness to noise.

C. Results on Real Datasets

1) *Dataset Description:* The Samson dataset³ is extensively used in unmixing, which contains 952×952 pixels, each with 156 spectral channels, covering the wavelength range from 401 nm to 889 nm, and the spectral resolution is up to 3.13 nm.

³http://www.escience.cn/people/feiyunZHU/Dataset_GT.html

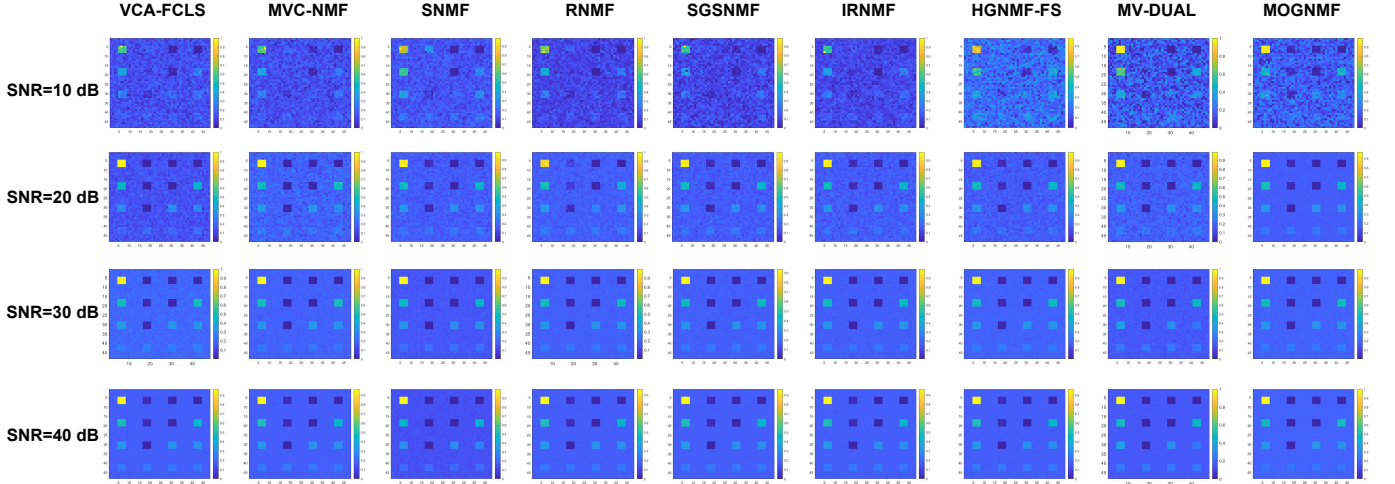


Fig. 6. Abundance maps of the endmember 1 obtained under different SNRs on the Simu-2 dataset.

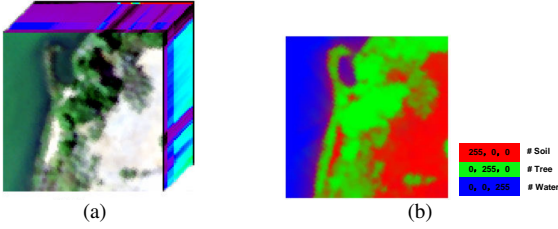


Fig. 7. Visualization of the Samson dataset, where (a) 3-D cube and (b) abundances.

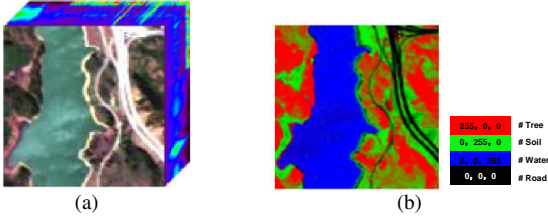


Fig. 8. Visualization of the Jasper Ridge dataset, where (a) 3-D cube and (b) abundances.

A subregion of 95×95 pixels starting at position (252, 332) is selected for analysis. Specifically, this image includes three targets, i.e., Soil, Tree, and Water, as shown in Fig. 7.

The Jasper Ridge dataset⁴ consists of 512×614 pixels, with each pixel recorded across 224 spectral channels covering a wavelength range from 380 nm to 2500 nm, and a spectral resolution of up to 9.46 nm. A subimage of 100×100 pixels is used for analysis. The endmembers include four categories: Tree, Soil, Water, and Road, as shown in Fig. 8.

2) *Numerical Results:* To demonstrate the performance of the proposed MOGNMF on real-world hyperspectral datasets, the SAD between the estimated endmembers and the reference spectra from the USGS spectral library is computed. The SAD values for MOGNMF and other compared methods on the Samson dataset are summarized in Table III. The results show that MOGNMF achieves better performance than competitors.

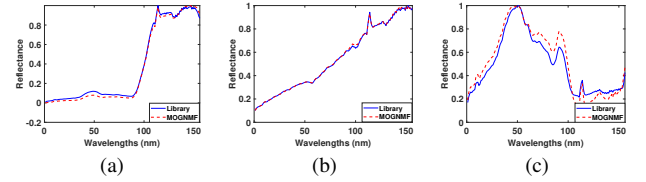


Fig. 9. Endmember signatures extracted by MOGNMF on the Samson dataset, where (a) Soil, (b) Tree, and (c) Water.

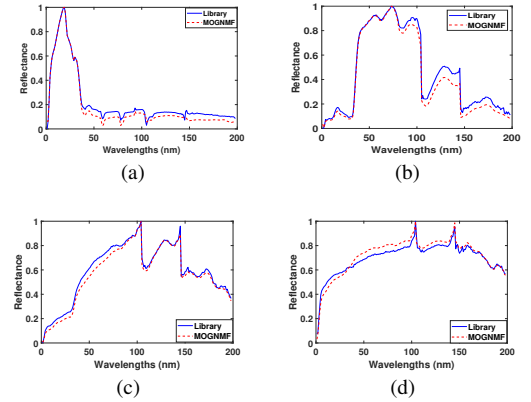


Fig. 10. Endmember signatures extracted by MOGNMF on the Jasper Ridge dataset, where (a) Tree, (b) Soil, (c) Water, and (d) Road.

To illustrate the capability of MOGNMF in extracting end-member signatures, Fig. 9 presents a comparison between the extracted signatures and the reference endmembers. The high degree of consistency between them validates the effectiveness of MOGNMF in the HU task. Besides, Table IV shows the resulting SAD obtained by different methods on the Jasper Ridge dataset. It can be observed that our proposed MOGNMF also achieves a lower average SAD value than others. Fig. 10 presents a comparison between the endmember signatures extracted by MOGNMF and the reference endmember signatures, demonstrating that MOGNMF can accurately extract spectral features and effectively distinguish different endmem-

⁴<http://www.escience.cn/system/file?fileId=68574>

TABLE III
SAD COMPARISONS FOR THE SAMON DATASET, WHERE THE TOP TWO VALUES ARE MARKED AS **RED** AND **BLUE**.

Cases	VCA-FCLS	MVC-NMF	SNMF	RNMF	SGSNMF	IRNMF	HGNMF-FS	MV-DUAL	MOGNMF
Soil	0.0447	0.0649	0.0129	0.0286	0.0209	0.0166	0.0237	0.0265	0.0094
Tree	0.0434	0.0532	0.0351	0.0716	0.0443	0.0374	0.0419	0.0386	0.0368
Water	0.1045	0.1208	0.1802	0.1389	0.0979	0.1045	0.0977	0.0715	0.0858
Average	0.0642	0.0796	0.0761	0.124	0.0544	0.0528	0.0544	0.0455	0.0447

TABLE IV
SAD COMPARISONS FOR THE JASPER RIDGE DATASET, WHERE THE TOP TWO VALUES ARE MARKED AS **RED** AND **BLUE**.

Cases	VCA-FCLS	MVC-NMF	SNMF	RNMF	SGSNMF	IRNMF	HGNMF-FS	MV-DUAL	MOGNMF
Tree	0.1369	0.1149	0.1370	0.1441	0.0970	0.0967	0.0810	0.1068	0.0776
Soil	0.1367	0.1826	0.1215	0.1328	0.1572	0.1554	0.1187	0.3781	0.1147
Water	0.1066	0.0617	0.0932	0.1052	0.0455	0.0454	0.0543	0.0407	0.0374
Road	0.0559	0.0303	0.0754	0.0664	0.0315	0.0283	0.0335	0.0427	0.0279
Average	0.1090	0.0974	0.1068	0.1121	0.0828	0.0814	0.0696	0.1421	0.0644

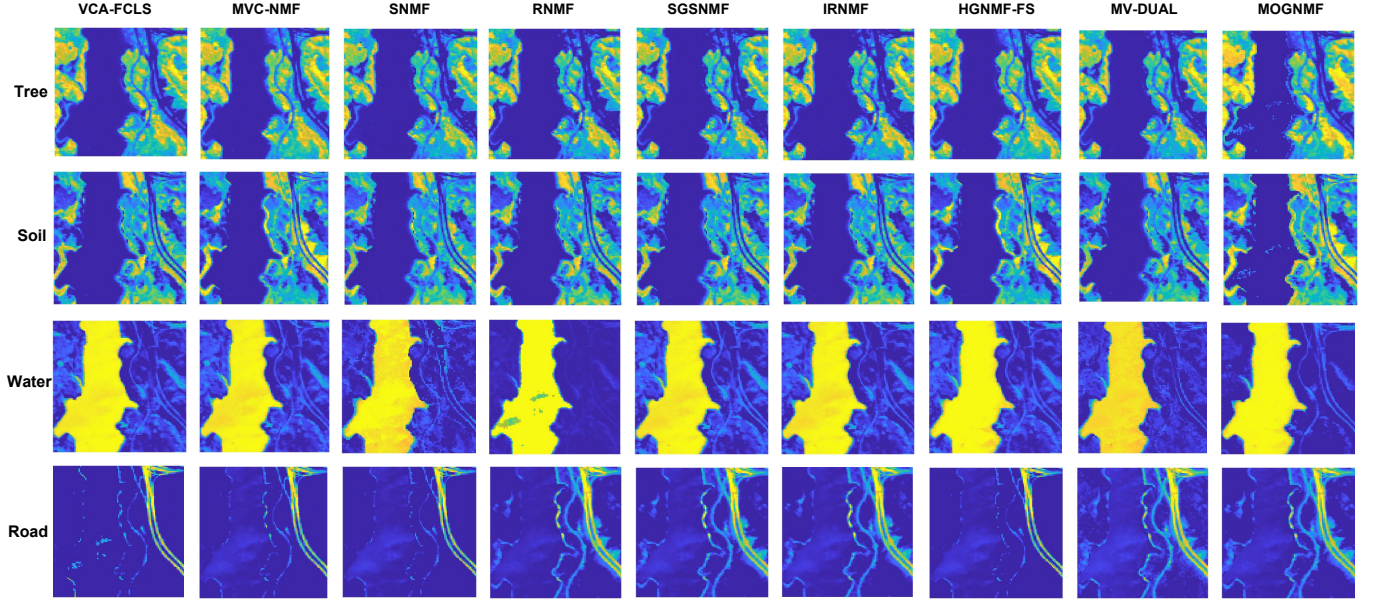


Fig. 11. Abundance map comparisons for the Samson dataset.

ber components.

Furthermore, Fig. 11 presents the abundance maps estimated by various methods on the Samson dataset, where blue represents lower abundance values, and yellow represents higher abundance values, which closely match the overall distribution trend of the reference map. The proposed MOGNMF demonstrates significant advantages in preserving spatial details and more naturally handling boundary transitions. For the Soil components, the proposed MOGNMF excels in retaining the edge details of the Soil regions, providing smoother transitions, and avoiding excessive sparsity or over-concentration in certain areas. In contrast, VCA-FCLS and MVC-NMF show blurring at the boundaries of Soil regions, with noticeable regional errors in abundance distribution, while IRNMF and SGSNMF exhibit overestimation or underestimation. These observations highlight the advantages of the multi-order graph regularization in the proposed MOGNMF. Additionally, Fig. 12 shows the abundance maps estimated by various methods

on the Jasper Ridge dataset. The abundance maps obtained by our proposed MOGNMF are highly consistent with the true distribution, effectively recovering the true abundance distribution of the hyperspectral data.

D. Ablation Studies

In this subsection, ablation experiments are conducted to verify the effectiveness of the multi-order graph and sparsity in our proposed MOGNMF. We first analyze the impact by removing different regularization terms as

- Case I: The proposed MOGNMF (also (15))

$$\min_{\mathbf{A}, \mathbf{S}, \mathbf{E}} \frac{1}{2} \|\mathbf{X} - \mathbf{E} - \mathbf{AS}\|_F^2 + \gamma \|\mathbf{S}\|_{1/2} + \beta \|\mathbf{E}\|_{2,1} + \frac{\lambda}{2} \text{Tr}(\mathbf{SL}_m \mathbf{S}^\top). \quad (38)$$

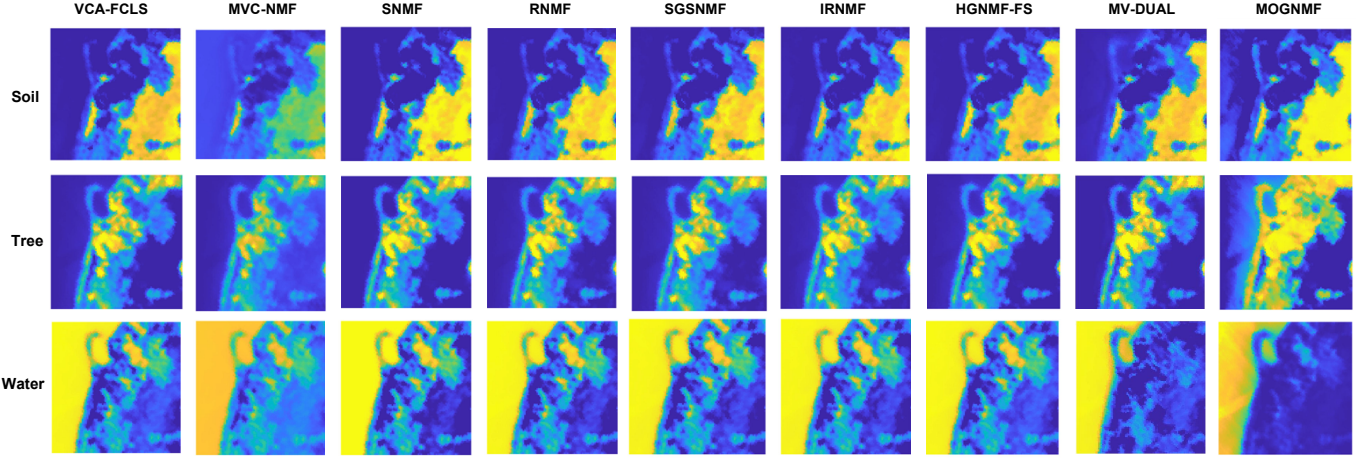


Fig. 12. Abundance map comparisons for the Jasper Ridge dataset.

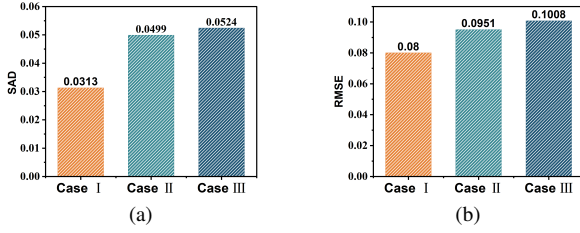


Fig. 13. Ablation comparisons of regularization terms on the Simu-1 dataset, where (a) SAD and (b) RMSE.

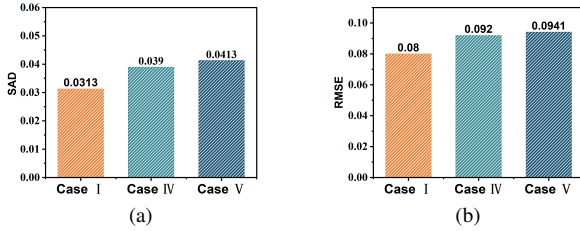


Fig. 14. Ablation comparisons of graph regularization orders on the Simu-1 dataset, where (a) SAD and (b) RMSE.

- Case II: The proposed MOGNMF *without* the noise matrix term

$$\min_{\mathbf{A}, \mathbf{S}} \frac{1}{2} \|\mathbf{X} - \mathbf{AS}\|_F^2 + \gamma \|\mathbf{S}\|_{1/2} + \frac{\lambda}{2} \text{Tr}(\mathbf{SL}_m \mathbf{S}^\top). \quad (39)$$

- Case III: The proposed MOGNMF *without* the noise matrix term and graph regularization term

$$\min_{\mathbf{A}, \mathbf{S}} \frac{1}{2} \|\mathbf{X} - \mathbf{AS}\|_F^2 + \gamma \|\mathbf{S}\|_{1/2}. \quad (40)$$

Fig. 13 presents the ablation results on the Simu-1 dataset with SNR = 20 dB. It can be observed that, compared with the two simplified models in Case II and Case III, our proposed MOGNMF in Case I achieves better performance in the unmixing task, demonstrating the importance and effectiveness of combining all three regularization terms.

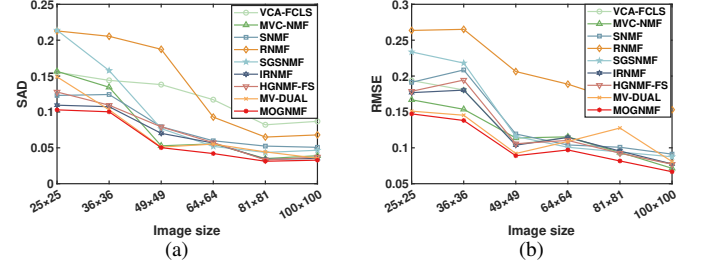


Fig. 15. Impact of image sizes, where (a) SAD and (b) RMSE.

Next, we analyze the unmixing results when only using the first-order and second-order nearest neighbor relationships by comparing Case I and the following two models

- Case IV: The proposed MOGNMF *with* an only second-order graph regularization term

$$\min_{\mathbf{A}, \mathbf{S}, \mathbf{E}} \frac{1}{2} \|\mathbf{X} - \mathbf{E} - \mathbf{AS}\|_F^2 + \gamma \|\mathbf{S}\|_{1/2} + \beta \|\mathbf{E}\|_{2,1} + \frac{\lambda}{2} \text{Tr}(\mathbf{SL}_2 \mathbf{S}^\top). \quad (41)$$

- Case V: The proposed MOGNMF *with* an only first-order graph regularization term

$$\min_{\mathbf{A}, \mathbf{S}, \mathbf{E}} \frac{1}{2} \|\mathbf{X} - \mathbf{E} - \mathbf{AS}\|_F^2 + \gamma \|\mathbf{S}\|_{1/2} + \beta \|\mathbf{E}\|_{2,1} + \frac{\lambda}{2} \text{Tr}(\mathbf{SL}_1 \mathbf{S}^\top). \quad (42)$$

From Fig. 14, it is found that our proposed MOGNMF in Case I can still obtain better unmixing performance than Case IV and Case V, which highlights the superiority of the adaptive multi-order graph framework.

E. Discussion

This section discusses the impact of image sizes, impact of endmember numbers, and convergence on the Simu-1 dataset.

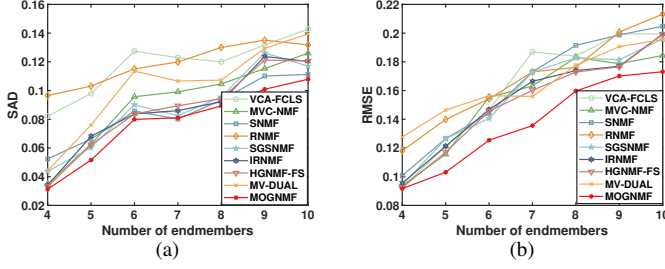


Fig. 16. Impact of endmember numbers, where (a) SAD and (b) RMSE.

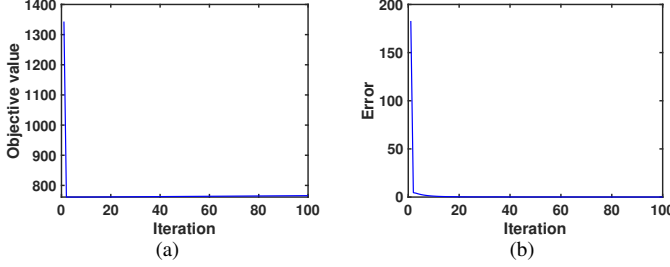


Fig. 17. Convergence analysis, where (a) Objective values and (b) Error.

1) *Impact of Image Sizes*: This experiment aims to evaluate the sensitivity to different image sizes, where the SNR is set to 20 dB, the number of endmembers is fixed to 9, and the image sizes are set to 30×30 , 40×40 , 50×50 , 60×60 , 80×80 , and 100×100 . As shown in Fig. 15, as the number of pixels increases, SGSNMF achieves better unmixing performance than SNMF, which is mainly attributed to its integration of spatial group structure and abundance sparsity. Our proposed MOGNMF, by incorporating the multi-order graph and dual sparsity, demonstrates greater adaptability and unmixing capability when handling HSIs with different pixel counts.

2) *Impact of Endmember Numbers*: To evaluate the performance under different numbers of endmembers, the SNR is set to 20 dB, and the number of endmembers ranges from 4 to 10. As shown in Fig. 16, the overall unmixing accuracy improves when the number of endmembers increases. This is because a larger number of endmembers introduces greater spectral mixing complexity, requiring the separation of more spectral features. Nevertheless, our proposed MOGNMF outperforms other compared methods in most cases, illustrating greater potential in unmixing.

3) *Convergence Analysis*: This study is conducted with 5 endmembers and the SNR ratio of 20. Fig. 17 shows that as the number of iterations increases, the objective function value decreases rapidly and gradually stabilizes. In addition, the relative error versus the number of iterations is provided, demonstrating the good convergence behavior.

VI. CONCLUSION

In this paper, we have provided a novel HU method called adaptive multi-order graph regularized NMF (MOGNMF), which successfully introduces multi-order graph regularization from both spatial and spectral perspectives, and obtains the optimal higher-order Laplacian through iterative optimization.

This method effectively addresses the challenges of order and parameter selection in traditional graph learning-based NMF methods. Extensive verification shows the superior performance of such adaptive multi-order graph learning. In addition, dual sparsity with $\ell_{1/2}$ -norm and $\ell_{2,1}$ -norm is incorporated, and its effectiveness has been verified by ablation experiments. To our best knowledge, this is the first time that integrates adaptive multi-order graph and dual sparsity into the NMF framework, with promising performance in HU.

In future work, we are interested in extending it to tensor cases and leveraging neural networks to learn prior structures.

REFERENCES

- [1] T. Dong, M. Wang, J. Pan, and Q. Wu, "Hyperspectral image intensity adaptive destriping method based on reference image-guided pixel clustering," *IEEE Transactions on Geoscience and Remote Sensing*, vol. 63, pp. 1–18, 2025.
- [2] Y. Chen, J. Zeng, W. He, X.-L. Zhao, T.-X. Jiang, and Q. Huang, "Fast large-scale hyperspectral image denoising via non-iterative low-rank subspace representation," *IEEE Transactions on Geoscience and Remote Sensing*, vol. 62, pp. 1–14, 2024.
- [3] Q. Zhang, Y. Zheng, Q. Yuan, M. Song, H. Yu, and Y. Xiao, "Hyperspectral image denoising: From model-driven, data-driven, to model-data-driven," *IEEE Transactions on Neural Networks and Learning Systems*, vol. 35, no. 10, pp. 13 143–13 163, 2024.
- [4] X. Nie, Z. Xue, C. Lin, L. Zhang, and H. Su, "Structure-prior-constrained low-rank and sparse representation with discriminative incremental dictionary for hyperspectral image classification," *IEEE Transactions on Geoscience and Remote Sensing*, vol. 62, pp. 1–19, 2024.
- [5] Y. Li, Y. Luo, L. Zhang, Z. Wang, and B. Du, "MambaHSI: Spatial-spectral Mamba for hyperspectral image classification," *IEEE Transactions on Geoscience and Remote Sensing*, vol. 62, pp. 1–16, 2024.
- [6] D. Datta, P. K. Mallick, A. K. Bhoi, M. F. Ijaz, J. Shafi, and J. Choi, "Hyperspectral image classification: Potentials, challenges, and future directions," *Computational Intelligence and Neuroscience*, vol. 2022, no. 1, p. 3854635, 2022.
- [7] J. Zhang, P. Xiang, J. Shi, X. Teng, D. Zhao, H. Zhou, H. Li, and J. Song, "A light CNN based on residual learning and background estimation for hyperspectral anomaly detection," *International Journal of Applied Earth Observation and Geoinformation*, vol. 132, p. 104069, 2024.
- [8] Q. Xiao, L. Zhao, S. Chen, and X. Li, "Hyperspectral anomaly detection via enhanced low-rank and smoothness fusion regularization plus saliency prior," *IEEE Journal of Selected Topics in Applied Earth Observations and Remote Sensing*, vol. 17, no. 12, pp. 18 987–19 002, 2024.
- [9] J. Liu, J. Jin, X. Xiu, W. Liu, and J. Zhang, "Exploiting weighted multidirectional sparsity for prior enhanced anomaly detection in hyperspectral images," *Remote Sensing*, vol. 17, no. 4, p. 602, 2025.
- [10] B. Rasti, A. Zouaoui, J. Mairal, and J. Chanussot, "Image processing and machine learning for hyperspectral unmixing: An overview and the hysupp python package," *IEEE Transactions on Geoscience and Remote Sensing*, vol. 62, pp. 1–31, 2024.
- [11] H. Li, D. Li, M. Gong, J. Li, A. K. Qin, L. Xing, and F. Xie, "Sparse hyperspectral unmixing with preference-based evolutionary multiobjective multitasking optimization," *IEEE Transactions on Emerging Topics in Computational Intelligence*, vol. 8, no. 2, pp. 1922–1937, 2024.
- [12] W. Gao, J. Yang, Y. Zhang, Y. Akoudad, and J. Chen, "SSAF-Net: A spatial-spectral adaptive fusion network for hyperspectral unmixing with endmember variability," *IEEE Transactions on Geoscience and Remote Sensing*, vol. 63, pp. 1–15, 2025.
- [13] A. ul Rehman and S. A. Qureshi, "A review of the medical hyperspectral imaging systems and unmixing algorithms' in biological tissues," *Photodiagnosis and Photodynamic Therapy*, vol. 33, p. 102165, 2021.
- [14] Ç. Esi, A. Ertürk, and E. Erten, "Nonnegative matrix factorization-based environmental monitoring of marine mucilage," *International Journal of Remote Sensing*, vol. 45, no. 11, pp. 3764–3788, 2024.
- [15] B. G. Ram, P. Oduor, C. Igathinathane, K. Howatt, and X. Sun, "A systematic review of hyperspectral imaging in precision agriculture: Analysis of its current state and future prospects," *Computers and Electronics in Agriculture*, vol. 222, p. 109037, 2024.

- [16] J. Li, A. Agathos, D. Zaharie, J. M. Bioucas-Dias, A. Plaza, and X. Li, "Minimum volume simplex analysis: A fast algorithm for linear hyperspectral unmixing," *IEEE Transactions on Geoscience and Remote Sensing*, vol. 53, no. 9, pp. 5067–5082, 2015.
- [17] Y. Li and T. Tan, "An initially robust minimum simplex volume-based method for linear hyperspectral unmixing," *International Journal of Remote Sensing*, vol. 45, no. 4, pp. 1033–1058, 2024.
- [18] N. Wang, B. Du, L. Zhang, and L. Zhang, "An abundance characteristic-based independent component analysis for hyperspectral unmixing," *IEEE Transactions on Geoscience and Remote Sensing*, vol. 53, no. 1, pp. 416–428, 2014.
- [19] X. Lu, L. Dong, and Y. Yuan, "Subspace clustering constrained sparse NMF for hyperspectral unmixing," *IEEE Transactions on Geoscience and Remote Sensing*, vol. 58, no. 5, pp. 3007–3019, 2019.
- [20] T. Ince, "Superpixel-based graph laplacian regularization for sparse hyperspectral unmixing," *IEEE Geoscience and Remote Sensing Letters*, vol. 19, pp. 1–5, 2020.
- [21] C. Deng, Y. Chen, S. Zhang, F. Li, P. Lai, D. Su, M. Hu, and S. Wang, "Robust dual spatial weighted sparse unmixing for remotely sensed hyperspectral imagery," *Remote Sensing*, vol. 15, no. 16, p. 4056, 2023.
- [22] V. S. Deshpande, J. S. Bhatt *et al.*, "A practical approach for hyperspectral unmixing using deep learning," *IEEE Geoscience and Remote Sensing Letters*, vol. 19, pp. 1–5, 2021.
- [23] X. Chen, X. Zhang, M. Ren, B. Zhou, Z. Feng, and J. Cheng, "An improved hyperspectral unmixing approach based on a spatial-spectral adaptive nonlinear unmixing network," *IEEE Journal of Selected Topics in Applied Earth Observations and Remote Sensing*, vol. 16, pp. 9680–9696, 2023.
- [24] J. M. Nascimento and J. M. Dias, "Vertex component analysis: A fast algorithm to unmix hyperspectral data," *IEEE Transactions on Geoscience and Remote Sensing*, vol. 43, no. 4, pp. 898–910, 2005.
- [25] D. C. Heinz and C. I. Chang, "Fully constrained least squares linear spectral mixture analysis method for material quantification in hyperspectral imagery," *IEEE Transactions on Geoscience and Remote Sensing*, vol. 39, no. 3, pp. 529–545, 2001.
- [26] D. D. Lee and H. S. Seung, "Learning the parts of objects by non-negative matrix factorization," *Nature*, vol. 401, no. 6755, pp. 788–791, 1999.
- [27] N. Gillis, *Nonnegative matrix factorization*. SIAM, 2020.
- [28] X.-R. Feng, H.-C. Li, R. Wang, Q. Du, X. Jia, and A. Plaza, "Hyperspectral unmixing based on nonnegative matrix factorization: A comprehensive review," *IEEE Journal of Selected Topics in Applied Earth Observations and Remote Sensing*, vol. 15, pp. 4414–4436, 2022.
- [29] L. Miao and H. Qi, "Endmember extraction from highly mixed data using minimum volume constrained nonnegative matrix factorization," *IEEE Transactions on Geoscience and Remote Sensing*, vol. 45, no. 3, pp. 765–777, 2007.
- [30] Y. Qian, S. Jia, J. Zhou, and A. Robles-Kelly, "Hyperspectral unmixing via $\ell_{1/2}$ sparsity-constrained nonnegative matrix factorization," *IEEE Transactions on Geoscience and Remote Sensing*, vol. 49, no. 11, pp. 4282–4297, 2011.
- [31] Z. Xu, X. Chang, F. Xu, and H. Zhang, " $\ell_{1/2}$ regularization: A thresholding representation theory and a fast solver," *IEEE Transactions on Neural Networks and Learning Systems*, vol. 23, no. 7, pp. 1013–1027, 2012.
- [32] F. Zhu, Y. Wang, B. Fan, S. Xiang, G. Meng, and C. Pan, "Spectral unmixing via data-guided sparsity," *IEEE Transactions on Image Processing*, vol. 23, no. 12, pp. 5412–5427, 2014.
- [33] J. Liu, M. Feng, X. Xiu, W. Liu, and X. Zeng, "Efficient and robust sparse linear discriminant analysis for data classification," *IEEE Transactions on Emerging Topics in Computational Intelligence*, vol. 9, no. 1, pp. 617–629, 2025.
- [34] X. Wang, Y. Zhong, L. Zhang, and Y. Xu, "Spatial group sparsity regularized nonnegative matrix factorization for hyperspectral unmixing," *IEEE Transactions on Geoscience and Remote Sensing*, vol. 55, no. 11, pp. 6287–6304, 2017.
- [35] C. Ye, S. Liu, M. Xu, and Z. Yang, "Combining low-rank constraint for similar superpixels and total variation sparse unmixing for hyperspectral image," *International Journal of Remote Sensing*, vol. 43, no. 12, pp. 4331–4351, 2022.
- [36] C. Xu, "Spectral weighted sparse unmixing based on adaptive total variation and low-rank constraints," *Scientific Reports*, vol. 14, no. 1, p. 23705, 2024.
- [37] X. Liu, W. Xia, B. Wang, and L. Zhang, "An approach based on constrained nonnegative matrix factorization to unmix hyperspectral data," *IEEE Transactions on Geoscience and Remote Sensing*, vol. 49, no. 2, pp. 757–772, 2010.
- [38] R. Liu, B. Du, and L. Zhang, "Hyperspectral unmixing via double abundance characteristics constraints based NMF," *Remote Sensing*, vol. 8, no. 6, p. 464, 2016.
- [39] Z. Li, J. Tang, and X. He, "Robust structured nonnegative matrix factorization for image representation," *IEEE Transactions on Neural Networks and Learning Systems*, vol. 29, no. 5, pp. 1947–1960, 2017.
- [40] S. Peng, W. Ser, B. Chen, and Z. Lin, "Robust semi-supervised non-negative matrix factorization for image clustering," *Pattern Recognition*, vol. 111, p. 107683, 2021.
- [41] C. Févotte and N. Dobigeon, "Nonlinear hyperspectral unmixing with robust nonnegative matrix factorization," *IEEE Transactions on Image Processing*, vol. 24, no. 12, pp. 4810–4819, 2015.
- [42] X. Zhang, X. Li, and C. Zhang, "Matrix optimization problem involving group sparsity and nonnegativity constraints," *Journal of Optimization Theory and Applications*, vol. 201, no. 1, pp. 130–176, 2024.
- [43] M. Abdolali, G. Barbarino, and N. Gillis, "Dual simplex volume maximization for simplex-structured matrix factorization," *SIAM Journal on Imaging Sciences*, vol. 17, no. 4, pp. 2362–2391, 2024.
- [44] Y. Duan, H. Huang, and Y. Tang, "Local constraint-based sparse manifold hypergraph learning for dimensionality reduction of hyperspectral image," *IEEE Transactions on Geoscience and Remote Sensing*, vol. 59, no. 1, pp. 613–628, 2020.
- [45] Z. Guo, A. Min, B. Yang, J. Chen, H. Li, and J. Gao, "A sparse oblique-manifold nonnegative matrix factorization for hyperspectral unmixing," *IEEE Transactions on Geoscience and Remote Sensing*, vol. 60, pp. 1–13, 2021.
- [46] X. Lu, H. Wu, Y. Yuan, P. Yan, and X. Li, "Manifold regularized sparse NMF for hyperspectral unmixing," *IEEE Transactions on Geoscience and Remote Sensing*, vol. 51, no. 5, pp. 2815–2826, 2012.
- [47] S. Yang, X. Zhang, Y. Yao, S. Cheng, and L. Jiao, "Geometric nonnegative matrix factorization for hyperspectral unmixing," *IEEE Journal of Selected Topics in Applied Earth Observations and Remote Sensing*, vol. 8, no. 6, pp. 2696–2703, 2015.
- [48] W. Wang, Y. Qian, and Y. Y. Tang, "Hypergraph-regularized sparse NMF for hyperspectral unmixing," *IEEE Journal of Selected Topics in Applied Earth Observations and Remote Sensing*, vol. 9, no. 2, pp. 681–694, 2016.
- [49] K. Qu, Z. Li, C. Wang, F. Luo, and W. Bao, "Hyperspectral unmixing using higher-order graph regularized NMF with adaptive feature selection," *IEEE Transactions on Geoscience and Remote Sensing*, vol. 61, pp. 1–15, 2023.
- [50] M. Meilă and H. Zhang, "Manifold learning: What, how, and why," *Annual Review of Statistics and Its Application*, vol. 11, no. 1, pp. 393–417, 2024.
- [51] D. Lee and H. S. Seung, "Algorithms for non-negative matrix factorization," *Advances in Neural Information Processing Systems*, vol. 13, 2000.
- [52] D. Wu, W. Chang, J. Lu, F. Nie, R. Wang, and X. Li, "Adaptive-order proximity learning for graph-based clustering," *Pattern Recognition*, vol. 126, p. 108550, 2022.
- [53] G. Liu, Z. Lin, S. Yan, J. Sun, Y. Yu, and Y. Ma, "Robust recovery of subspace structures by low-rank representation," *IEEE Transactions on Pattern Analysis and Machine Intelligence*, vol. 35, no. 1, pp. 171–184, 2012.